Contemporary deformation of the Wasatch Fault, Utah, from GPS measurements with implications for interseismic fault behavior and earthquake hazard: Observations and kinematic analysis

Wu-Lung Chang,[1] Robert B. Smith,[1] Charles M. Meertens,[2] and Ron A. Harris[3]

Received 3 February 2006; revised 14 July 2006; accepted 1 August 2006; published 22 November 2006.

[1] Contemporary strain accumulation rates of the 350-km-long Wasatch fault, Utah, have been determined by GPS measurements and provide key data for evaluating normal fault behavior and related earthquake hazard assessment. This paper presents a complete description of the Wasatch GPS network, data archiving and processing, and the measured ground deformation. The network spans the Wasatch fault in an area ~300-km long and ~200-km wide in north and central Utah and consists of 43 GPS sites surveyed in 1992, 1993, 1994,1995, 1999, 2001, and 2003, plus 8 permanent GPS stations operating continuously beginning 1997. Observations across a 65-km wide area centered on the Wasatch fault indicate the principal horizontal extension rate of 24 ± 6 nstrain/yr with the direction nearly perpendicular to the fault. This strain rate corresponds to a horizontal displacement rate of 1.6 ± 0.4 mm/yr, accommodating ~50% of the crustal deformation across the ~200 km-wide eastern Basin-Range. Analysis of the spatial variation of the strain-rate field reveals that the strain accumulation is concentrated near the Wasatch fault, which suggests an abrupt transition in the horizontal deformation at the fault between the eastern Basin-Range and the Rocky Mountains. We employed a finite-strain model that accounts for simple-shear deformation of the hanging-wall to compare horizontal extension rates measured by GPS with vertical fault-displacement rates determined by geologic data. Our results suggest that the average Holocene strain-release rate is higher than the contemporary strain-loading rate for the Wasatch fault if the fault dips less than 30°W, but these two rates are consistent if the fault dips more steeply.

Citation: Chang, W.-L., R. B. Smith, C. M. Meertens, and R. A. Harris (2006), Contemporary deformation of the Wasatch Fault, Utah, from GPS measurements with implications for interseismic fault behavior and earthquake hazard: Observations and kinematic analysis, *J. Geophys. Res.*, *111*, B11405, doi:10.1029/2006JB004326.

1. Introduction

[2] It is generally accepted that stress and resulting strain accumulation on a fault is a time-dependent process during the earthquake cycle [e.g., *Thatcher*, 1983]. While geologic information such as paleoearthquake fault displacements from fault trenching have been used to determine average slip or strain-release rates, geodetic measurements provide contemporary strain-loading rates on faults. In this study, we present a comprehensive discussion on the acquisition and processing of GPS data of the Wasatch fault in northern and central Utah, and focus on accessing the contemporary ground deformation and the relation between geodetically and geologically observed strain rates.

[3] The 370 km-long, Late Quaternary Wasatch fault extends along the west side of the Wasatch Range, UT, and traverses the populated Wasatch Front area where more than 80% of Utah's two-million+ people reside, including the cities of Ogden, Salt Lake City, and Provo (Figure 1). The fault, generally interpreted to be composed of six Holocene segments, is part of the central Intermountain Seismic Belt that separates the stable Rocky Mountains and Colorado Plateau to the east and the extending lithosphere of the Basin and Range province to the west [*Smith and Sbar*, 1974; *Smith and Arabasz*, 1991].

[4] Based on analyses of fault morphology and Holocene rupture dating by trenching of the Wasatch fault, an excellent record of paleoearthquake history has been defined for the past 5,600 years [e.g., *Schwartz and Coppersmith*, 1984; *Machette et al.*, 1992; *McCalpin and Nishenko*, 1996; *Olig et al.*, 2004]. During this period the fault experienced 11 multi-segment scarp-forming paleoearthquakes ($6.8 < M < 7.2$) with the youngest rupture about 600 years ago on the Provo segment. Multiple studies of the geologic data, including determination of vertical fault displacements observed at

[1]Department of Geology and Geophysics, University of Utah, Salt Lake City, Utah, USA.
[2]University Navstar Consortium, Boulder, Colorado, USA.
[3]Department of Geology, Brigham Young University, Provo, Utah, USA.

0148-0227/06/2006JB004326$09.00

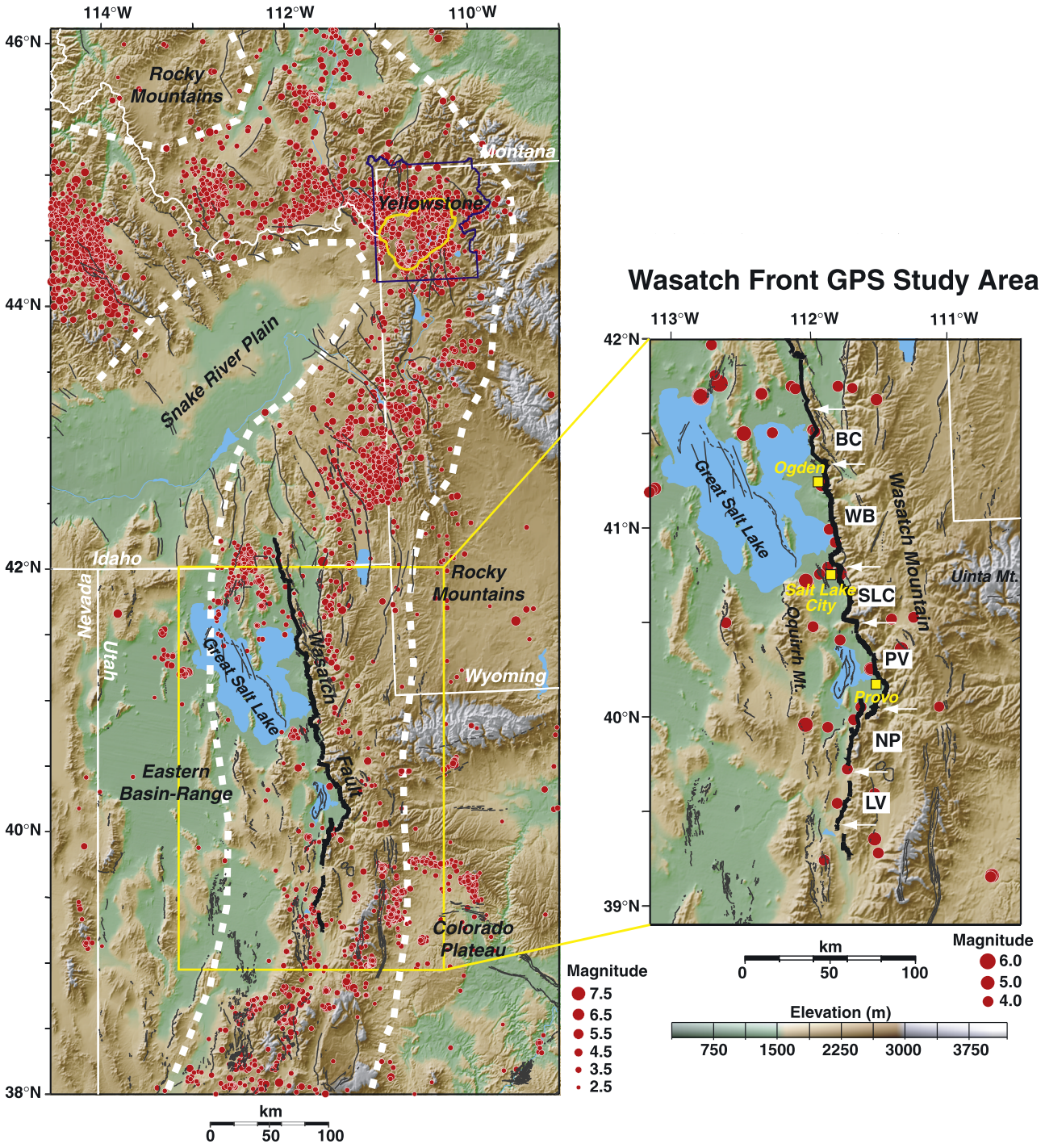

Figure 1. Seismicity map of the Intermountain Seismic Belt (white dashed lines) showing M $\geq$ 2 historic earthquakes. Thick black lines highlight the Quaternary Wasatch fault. Thin black lines show other Quaternary faults in the region. The Wasatch Front GPS study area with M $\geq$ 4 historic earthquakes is shown at the right. Six Holocene-active segments of the Wasatch fault are depicted: the Brigham City (BC), Weber (WB), Salt Lake City (SLC), Provo (PV), Nephi (NP), and Levan (LV). Yellow squares show major cities. Earthquake data are from the 1962–1996 University of Utah Seismograph Stations catalog.

14 trenches along the Wasatch fault, revealed Holocene fault slip rates of 1–2 mm/yr [*Hecker*, 1993; *Chang and Smith*, 2002; *Friedrich et al.*, 2003].

[5] In spite of the evidence of large, scarp-forming prehistoric ruptures on the Wasatch fault, it has only experienced small to moderate earthquakes in historic time (Figure 1), including 23 main shocks of $M_L \geq 4.0$ from 1900–1994, of which three were $M_L \geq 5.6$ [*Arabasz et al.*, 1992; *Pechmann and Arabasz*, 1995]. Seismic moment rates estimated from the instrumental earthquake record

correspond to relatively low strain-release rates of 1 to 4 nstrain/yr [*Eddington et al.*, 1987]. Notably these values are an order of magnitude smaller than the horizontal strain-loading rates of ~50 nstrain/yr implied by geodetic measurements from 1962 to 1995 [*Snay et al.*, 1984; *Savage et al.*, 1992; *Martinez et al.*, 1998]. This discrepancy suggests that historic earthquakes of the Wasatch area have only released a small fraction of the strain energy accumulated in this area.

[6] To better understand the contemporary behavior of the Wasatch fault and its implication to the earthquake hazard, we have collected and analyzed campaign (1992–1995, 1999, 2001) and continuous (1997–2004) GPS data along the Wasatch Front area. Details on our data processing scheme and results of ground motion and strain-rate analysis are presented in this paper. A finite-strain model for the hanging-wall deformation is employed to compare the horizontal deformation rate from GPS measurements and vertical fault displacement rate from paleoearthquake data. Knowledge of the relation between these two rates provides key information to the studies of the earthquake cycle and seismic hazards of the Wasatch fault.

2. Previous Geodetic Studies of the Wasatch Front, Utah

2.1. Triangulation and Trilateration Surveys

[7] Modern geodetic surveys for deformation rates of the Wasatch fault were first conducted by the National Ocean Service/National Geodetic Survey (NOS/NGS) across the central part of the fault (Figure 2): (1) for the period of 1962 to 1963 using triangulation surveys and (2) from 1973 to 1974 using combined triangulation-trilateration surveys [*Snay et al.*, 1984]. These data revealed principal horizontal extensional strain at a rate of 80 ± 30 nstrain/yr and an azimuth of 114° ± 15°. This rate corresponds to a horizontal crustal velocity of 2.4 ± 0.9 mm/yr across the ~30 km-wide network.

[8] In 1972, the U.S. Geological Survey (USGS) established a trilateration network spanning the Wasatch fault in the vicinity of Ogden, Utah. This network complemented the previous NOS/NGS geodetic network to the south (Figure 2). Distances between the geodetic benchmarks were measured from 1972 through 1990 with Geodolites, an electronic distance measurement (EDM) instrument providing an accuracy of ~4 mm for a baseline length of 10 km [*Savage and Prescott*, 1973]. Results from these surveys indicated a more definitive pattern of hanging-wall extension with a strain rate of 47 ± 11 nstrain/yr, oriented N83°E ± 5°, which corresponds to a horizontal velocity of 1.6 ± 0.4 mm/yr across a 40 km-wide zone west of the Wasatch fault [*Savage et al.*, 1992].

[9] Assuming an elastic dislocation for fault slip behavior, *Savage et al.* [1992] modeled the EDM data as the result of asesimic loading of a listric fault. Their model consisted of an upper and steeply dipping portion, 60°W, of the fault that was locked from the surface to a depth of 20 km, and a lower and shallow dipping portion, 10°W, extending indefinitely and slipping continuously below the locked portion. The 1981 to 1990 observations on the footwall-block east of the Wasatch fault, on the other hand, revealed a north-northeast direction of extension that was distinct from the strain field to the west of fault (Figure 2). *Savage et al.* [1992] attributed this difference to an artifact of systematic bias in the 1981 survey.

2.2. Global Positioning System (GPS) Measurements

[10] The above geodetic techniques resolved strain rates of the network by measuring temporal changes of baseline lengths. The Navigation Satellite Time and Ranging (NAVSTAR) Global Positioning System (GPS), on the other hand, is a satellite-based point-positioning system from which point locations can be estimated with an accuracy of about 2–4 mm for the horizontal component and approximately 10 mm for the vertical component in a global reference frame. Compared with the EDM technology, GPS can measure baseline length more accurately and has the advantage that the observation points need not be line-of-sight.

[11] The University of Utah initiated detailed GPS campaign surveys in 1992 to determine the contemporary deformation field across the Wasatch fault and evaluate the inter-seismic behavior and earthquake hazard of this large normal fault. A total of 107 campaign GPS sites, whose baselines spanned the Wasatch fault (Figure 2) with an average spacing of about 15 km, were occupied in 1992, 1993, 1994, and 1995 [*Martinez et al.*, 1998]. Data from these initial observations revealed an averaged east-west extensional strain at a rate of 49 ± 23 nstrain/yr, corresponding to a 2.7 ± 1.3 mm/yr horizontal displacement rate across a 55 km-wide fault zone. Within the error range, the result is similar to that from the previous triangulation-trilateration surveys and later GPS measurements introduced below.

[12] Regional-scale tectonic studies have employed GPS to investigate crustal deformation across parts of the Basin and Range province (abbreviated as Basin-Range in the following text) including the Wasatch area. *Dixon et al.* [2000], for example, used GPS data from five sites on the Sierra Nevada block to estimate its angular velocity relative to stable North America. With this velocity as a kinematic boundary condition, they modeled a nearly westward motion of 3.4 ± 1.2 mm/yr across the ~200 km-wide eastern Basin-Range, an extensional tectonic regime between the Utah-Nevada boarder and the Wasatch fault encompassing the Wasatch and several other secondary normal faults (Figure 2). This velocity is consistent with a rate of 4.9 ± 1.3 mm/yr determined by very long baseline interferometry (VLBI) between 1984 and 1990, and probably represents an upper limit for the rate of horizontal extension across the Wasatch fault zone [*Dixon et al.*, 2000].

[13] The California Institute of Technology and the Harvard Smithsonian Center of Astrophysics, more recently, established the Basin and Range geodetic network, or BARGEN. The network includes 18 widely-spaced, average spacing ~100 km, continuous GPS stations spanning roughly 800 km near latitude 40°N to study the crustal deformation of the Basin-Range province [*Bennett et al.*, 2003]. The 1996–2001 BARGEN data revealed an east-west extensional motion of 1.7 ± 0.2 mm/yr between two stations with a 65-km baseline across the Wasatch fault between HEBE and COON (Figure 2). This motion corresponds to a strain rate of 26 ± 1 nstrain/yr that is a factor of two larger than the rate across the eastern Basin-Range between two distant BARGEN stations HEBE and GOSH (Figure 2), indicating a concentration of strain accumulation near the Wasatch fault [*Friedrich et al.*, 2003].

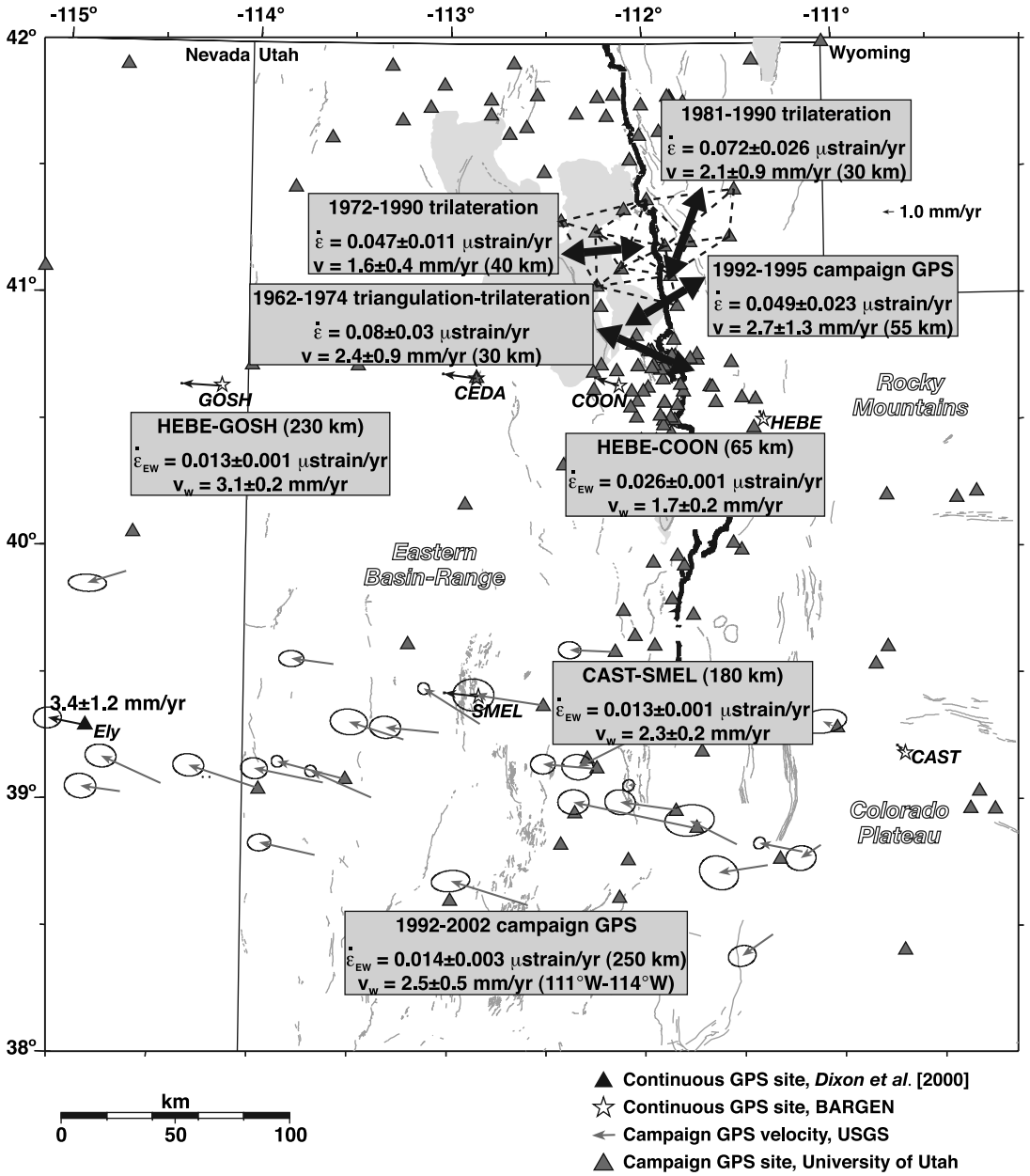

Figure 2. Geodetic determinations of ground deformation of the eastern Basin-Range province and the Wasatch Front, Utah, from (1) the 1962–1974 triangulation-trilateration network, *Snay et al.* [1984], (2) the 1972–1990 and 1981–1990 trilateration network, *Savage et al.* [1992], (3) the 1992–1995 campaign GPS network, *Martinez et al.* [1998], (4) the 1992–2002 USGS campaign GPS networks, *Thatcher et al.* [1999] and *Hammond and Thatcher* [2004], (5) the velocity at Ely, *Dixon et al.* [2000], and (6) the 1996–2001 continuous GPS network, *Bennett et al.* [2003]. Bold lines highlight the Wasatch fault. Dashed lines represent baselines of the trilateration network. $\dot{\varepsilon}_{EW}$ and V_w represent east-west strain rate and west velocity, respectively. The error ellipses represent the 95% confident intervals.

Here we emphasize that the Wasatch GPS network, used by this study and introduced in section 3, has 13 stations across the central Wasatch fault between HEBE and COON, from which we resolve the spatial strain variation associated with the fault in much more detail.

[14] In the southern Wasatch area, campaign GPS surveys of 90 sites were conducted by the USGS in 1992, 1996, 1998, and 2002, across the 800 km of Basin-Range between 39°N and 40°N (Figure 2) [*Thatcher et al.*, 1999; *Hammond and Thatcher*, 2004]. These measurements indicated an east-west extensional strain rate of 14 ± 3 nstrain/yr across an area between ~111°W and 114°W encompassing the southernmost part of the Wasatch fault. This rate corresponds to a horizontal velocity of 2.5 ± 0.5 mm/yr that is consistent with the relative velocity of 2.3 ± 0.2 mm/yr observed between two BARGEN stations CAST and SMEL

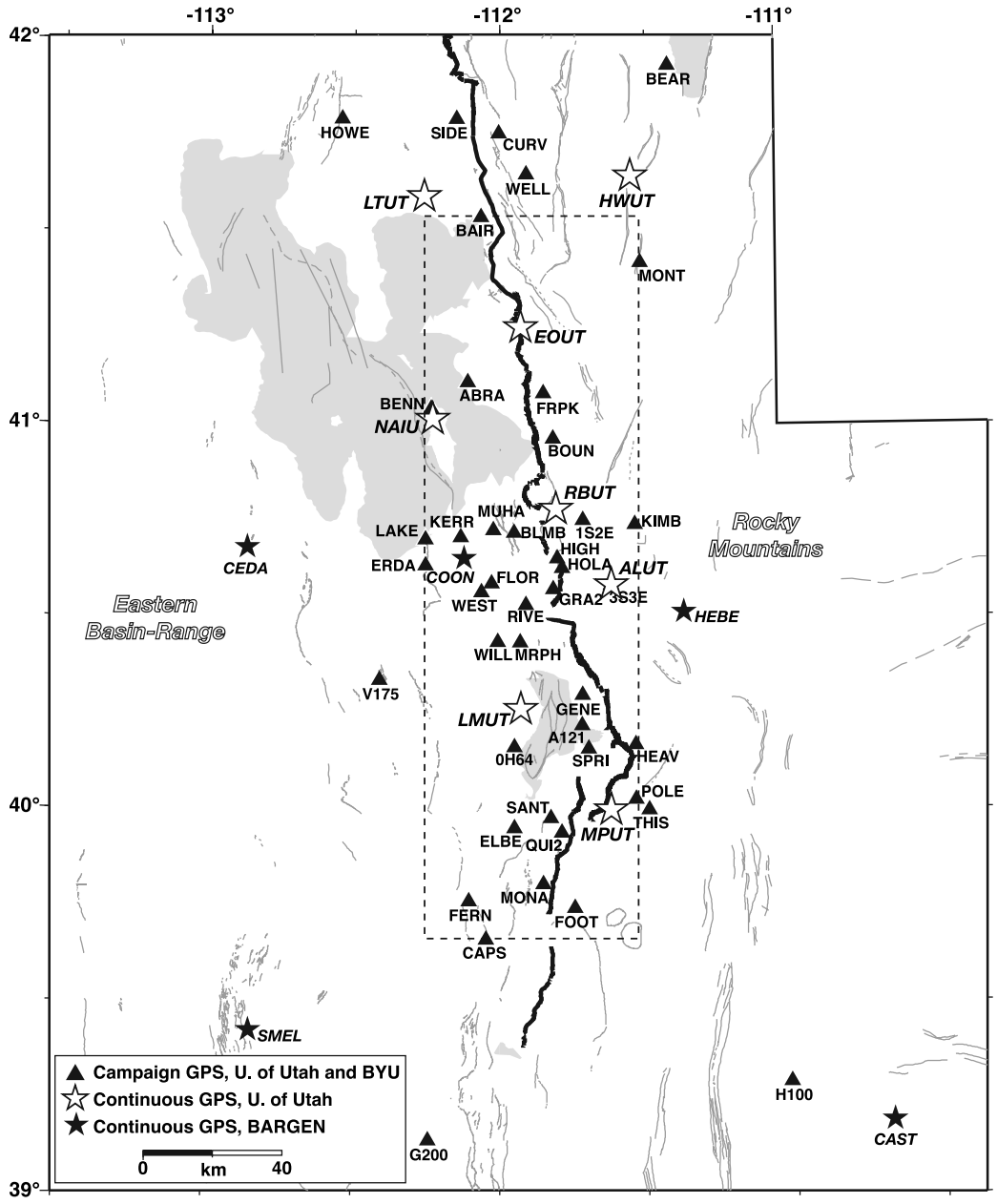

Figure 3. Wasatch Front GPS campaign (triangles) and continuous (stars) sites occupied and evaluated in this study. Bold lines highlight the Wasatch fault, and gray lines show other Quaternary faults. The dashed box indicates the Wasatch fault area shown in Figure 5.

spanning a 180-km baseline across the southernmost Wasatch and other faults (Figure 2) [*Niemi et al.*, 2004].

3. Wasatch GPS Network and Data Analysis

[15] The above geodetic measurements revealed east-west extensional deformation of about 3 mm/yr across the eastern Basin-Range, within which the Wasatch fault has been considered as the major active tectonic structure accommodating the deformation [e.g., *Hecker*, 1993; *Friedrich et al.*, 2003]. These geodetic studies, however, provided relatively poor spatial resolution for investigating the variation of the regional strain along the Wasatch fault. For example, *Friedrich et al.* [2003] and *Niemi et al.* [2004] used data from only two to three GPS stations distributed in lines over 130-km long across the fault.

[16] In this study, data from the Wasatch GPS network are shown to increase the resolution for determining local strain accumulation across the Wasatch fault. This spatially dense network consists of 107 campaign and 8 permanent stations, primarily located within a 65 km-wide and 200 km-long area spanning the fault with data recorded since 1992 (Figure 3). In sections 3.1–3.4 we introduce the network in detail.

3.1. Campaign GPS Measurements

[17] Following the initial GPS surveys reported by *Martinez et al.* [1998] for the Wasatch area, three additional GPS

campaign surveys re-occupying 43 sites in 1999, 2001, and 2003 (Figure 3, see the auxiliary material for detailed station descriptions) were conducted by the University of Utah with the assistance of the staff and students of Brigham Young University and staff of the Utah Geological Survey and the Bureau of Land Management.[1] These surveys increase the time span of the previous observations from 4 years to 11 years and considerably improve the precision of the velocity estimation by a factor of as much as 4 to 5 [*Brockmann*, 1996].

[18] Our campaign GPS surveys referred to observations at previously established benchmarks or horizontal control points of the NGS, USGS and local surveying groups. These sites were occupied for a few days to weeks once every year or more in a temporary deployment of GPS receivers. At least 16 hours of data were recorded for each station during one or two Julian days in each campaign year, with the sampling rate of 30 s. Most of the monuments are disks in concrete or bedrock firmly attached to the ground, except one site BLMB that is a threaded rod on a concrete pillar of a building (see the auxiliary material).

[19] For early surveys between 1992 and 1995 prior to the establishment of the Wasatch continuous GPS network, at least one and up to three base stations were operated continuously during the period of each campaign such that station coordinates can be solved and loosely constrained to a local reference frame determined by the base stations. Beginning in 1999, Wasatch continuous GPS stations were used as the reference stations.

3.2. Continuous GPS Measurements

[20] While campaign surveys can provide denser areal coverage in larger areas and thus enhance the spatial resolution of regional velocity field, continuously operating GPS measurements yield daily estimates of site positions with higher accuracies than campaign data because of their longer observation intervals (24 hours/day compared with 8 hours/d), fewer human errors from improper instrument operations, and more stable monuments used (e.g., invar rod installations in bedrock and Wyatt-type deep drilled and braced monuments [*Wyatt*, 1982]). The continuous data provide horizontal and vertical precisions of 2–4 mm and ~1 cm, respectively, over regional distances in global frame but are not as spatially dense as campaign GPS observations.

[21] Beginning in 1996, the University of Utah began installing a total of eight permanent GPS stations spanning the Wasatch fault, of which four stations, RBUT, NAIU, LMUT, and EOUT, have operated for more than 6 years (Figure 3). Four newer sites, MPUT, LTUT, HWUT, and ALUT, were installed after 2002 but were not used in this study due to their relatively higher velocity errors (formal errors >0.5 mm/yr compared with ~0.1 mm/yr for sites running 6 years). The station descriptions and parametric data of all of the University of Utah GPS campaign and continuous sites are documented in the auxiliary material and the data are archived at UNAVCO (http://www.unavco.org).

[22] In addition, data from five GPS stations of the BARGEN network were also included in this study (Figure 3, also documented in the auxiliary material). We thus employed data from a total of nine continuous sites for determining baseline changes across the footwall and hanging-wall blocks of the Wasatch fault. All the continuous GPS monuments were installed on bedrock in the surrounding mountains or on bedrock salients of the Wasatch fault so that their motions are most sensitive to tectonic signals from the Earth's crust and least contaminated by secular effects of hydrologic processes in the adjacent basins.

[23] Data from seven regional GPS stations of the International GNSS Service (IGS, see the auxiliary material) were processed together with our GPS data for the purpose of tying the local coordinate solutions to a global reference frame-in this study we chose the ITRF2000 (see section 3.4). BARGEN and IGS data are archived at the UNAVCO and SOPAC (Scripps Orbit and Permanent Array Center) data archive centers, respectively.

3.3. GPS Instrumentation

[24] The University of Utah field campaigns employed Trimble 4000 (SST, SSE, SSI) dual frequency GPS receivers capable of recording the L1 and L2 phases of the satellite signal. While the SST model can only receive C/A code range and half wavelength of L2 (full of L1) phase measurements, SSE and SSI were upgraded to record both C/A and P codes and full wavelength of both L1 and L2 phases. The SSI receiver, in addition, was a state-of-the-art model that had better satellite tracking and multi-path reduction than SSE.

[25] The 1992 Wasatch campaign employed 4000 SST receivers, while the 1993–1995 campaigns included a mixture of the SSE, SST, and SSI models. The 1999, 2001, and 2003 field data were collected using only SSI receivers. The four continuous GPS stations used in this study were equipped with SSI receivers.

[26] Three models of Trimble antennas were used for the Wasatch campaigns: the 4000 SST L1/L2 Geodetic (SST), 4000 SSE L1/L2 Compact with Ground Plane (SSE), and Dorne-Margolin (Choke Ring). While only SST antennas were available for the first two Wasatch GPS campaigns, the combination of SST and SSE models was employed in 1994 and 1995. In the 1999, 2001, and 2003 surveys, the newly developed Choke Ring antennas, designed to suppress the multipath signal reflected from objects below the antenna, were used at all sites. This type of antenna was also used at all Wasatch continuous GPS stations.

3.4. Data Processing and Reference Frame

[27] We employed the Bernese 4.2 GPS data processing algorithm [*Hugentobler et al.*, 2001] to process the campaign and continuous GPS data to obtain the daily station coordinates. Key steps in the processing scheme, including the selection of satellite orbit files and strategies of resolving initial phase ambiguities, are described in the auxiliary material.

[28] In the final output of the data processing, the station coordinates were constrained to a global reference frame ITRF (International Terrestrial Reference Frame) that was determined by the geocentric coordinates and velocity fields of IERS (International Earth Rotation Service) tracking stations from various space techniques (e.g., VLBI, satellite laser ranging (SLR), and GPS) and was mainly independent of plate tectonic models [*Sillard et al.*, 1998]. We constrained

[1] Auxiliary material data sets are available at ftp://ftp.agu.org/apend/jb/2006jb004326. Other auxiliary material files are in the HTML.

the GPS coordinate solutions described in this paper to the most recent global reference frame of ITRF2000.

4. Kinematic GPS Velocity and Strain-Rate Analysis

4.1. Velocity Estimate and Error Analysis

[29] Figure 4 shows the three-component time series of daily coordinate changes at the four Wasatch continuous GPS stations from 1997.0 to 2004.1 (in decimal years). Station position changes with respect to the global velocity frame of ITRF2000 were removed from these time series, so that the trends provide the estimates of regional ground velocities.

[30] Notably, these time series, especially the horizontal components, reveal short-term periodic (mostly annual) signals that are thought to be related to mechanisms such as seasonal fluctuation of local groundwater table [e.g., *Bawden et al.*, 2001], or global mode of Earth deformation due to redistribution of surface load [e.g., *Blewitt et al.*, 2001]. *Blewitt and Lavallée* [2002] found the annual variation of GPS site coordinates with typical amplitudes of 2–4 mm for horizontal and 4–8 mm for vertical, which are similar to the magnitudes of periodic signals shown in Figure 4. *Blewitt and Lavallée* [2002] also pointed out that 2.5 years would be a minimum data span to neglect the effect of annual signal on velocity solutions. Since all GPS data used in this study were recorded longer than 2.5 years, linear (or steady-state) motion of station coordinates was assumed as a first-order approximation to determine point velocities.

[31] Based on this premise, we used the ADDNEQ algorithm [*Brockmann*, 1996] within the Bernese 4.2 software to combine daily coordinate solutions and covariance matrices to solve for the site velocities. The method of ADDNEQ assumes that the daily station coordinates are a linear function of time during the period of observation so that the station velocities can be solved according to the technique of least-squares estimation (LSE). ADDNEQ also applies the concept of sequential adjustment, in which the results of LSE using all observations in one step are the same as splitting up the LSE in different parts and combining the results in a latter step.

[32] We initially post-processed each daily normal-equation (NEQ) file output from Bernese, including pre-elimination of parameters such as unresolved ambiguities and troposphere residuals, estimation of weighting factors from coordinate covariance, and transforming station coordinates into a consistent reference frame. Station velocities were then set up as new parameters in NEQ and were solved in a manner of LSE by combining all updated NEQ files.

[33] Our modeled velocity field for the Wasatch area was determined relative to a stable North America (SNA) reference frame. This reference frame is in a rigid North America continental framework by minimizing the residual velocities of 45 sites assumed to define a stable North America interior [*Bennett et al.*, 2003]. Therefore, placing velocities into a SNA reference frame was assumed to reveal crustal motion with respect to the North America plate. In this study, the SNA reference frame was defined by fixing the velocities of the seven IGS stations to values from *Bennett et al.* [2003] (Table 1).

[34] When computing the errors of station velocities, ADDNEQ assumes that the daily coordinate estimates are uncorrelated so that only white-noise uncertainties are taken into account. The GPS time series shown in Figure 4, however, exhibits the existence of temporal correlations among daily coordinate solutions. Therefore the formal velocity error from ADDNEQ needs to be modified for the estimate of the "scaled" error that includes time-correlated, or "colored", noise [e.g., *Agnew*, 1992; *Mao et al.*, 1999; *Williams et al.*, 2004].

[35] We employed a chi-square test method to determine the scaled-errors of the Wasatch GPS velocities. This method is similar to that in *Davis et al.* [2003] and *Hammond and Thatcher* [2004] and is based on two assumptions. First, the change of the northern components of the GPS velocities is a linear function of the north-south distance across the Wasatch GPS network. This assumption is geologically plausible because the nearly north-striking and west-dipping Wasatch normal fault and the westward extension of the Basin-Range Province would produce lower variations in strain rate in the north-south direction. Accordingly, we next assumed that the all variations unexplained by the best-fitting linear model of the north velocity originate from uncertainty in our velocity estimate, so that the north velocity misfit provides an approximation to the scaled velocity error.

[36] The mean chi-square misfit of the north velocity as a linear function of the north-south distance can be formulated as

$$\chi^2 = \frac{1}{n-2}\sum_{i=1}^{n}\left(\frac{V_{o(i)} - V_{p(i)}}{\sigma_{(i)}}\right)^2, \qquad (1)$$

where n is the number of GPS stations, $V_{o(i)}$ is the north velocity observed at the ith station, $V_{p(i)}$ is the north velocity predicted from the linear regression model that best fits the observations, and $\sigma_{(i)}$ is the formal velocity error. Therefore we weighted the formal error $\sigma_{(i)}$ by a factor of $(\chi^2)^{1/2}$ for the estimate of the scaled error of the ith station.

[37] Because the continuous and campaign GPS observations may have different levels of noise; for example, the campaign data can poorly sample systematic noise such as annual variations, we calculated the scaled velocity uncertainty separately for these two measurement modes. Our results show that the scaling factors were 2.6 and 4.8 for the continuous and campaign Wasatch GPS velocities, respectively.

[38] The scaled-error described above is the upper bound of the true uncertainty in the velocity estimate since there could exist real variations in strain rate unaccounted by the linear velocity model, or the east-west uniaxial strain rate model. For example, seasonal fluctuation of ground water level may induce surface deformation greater in the center of a sedimentary basin than on its periphery [e.g., *Bawden et al.*, 2001]. Thus local strain-rate changes should not be treated as an error source on velocity estimate. Further error analysis of GPS measurements, such as those in the frequency domain [e.g., *Mao et al.*, 1999; *Williams et al.*, 2004], are needed to better understand the content of different time-correlated noise types and approach velocity uncertainties more realistically.

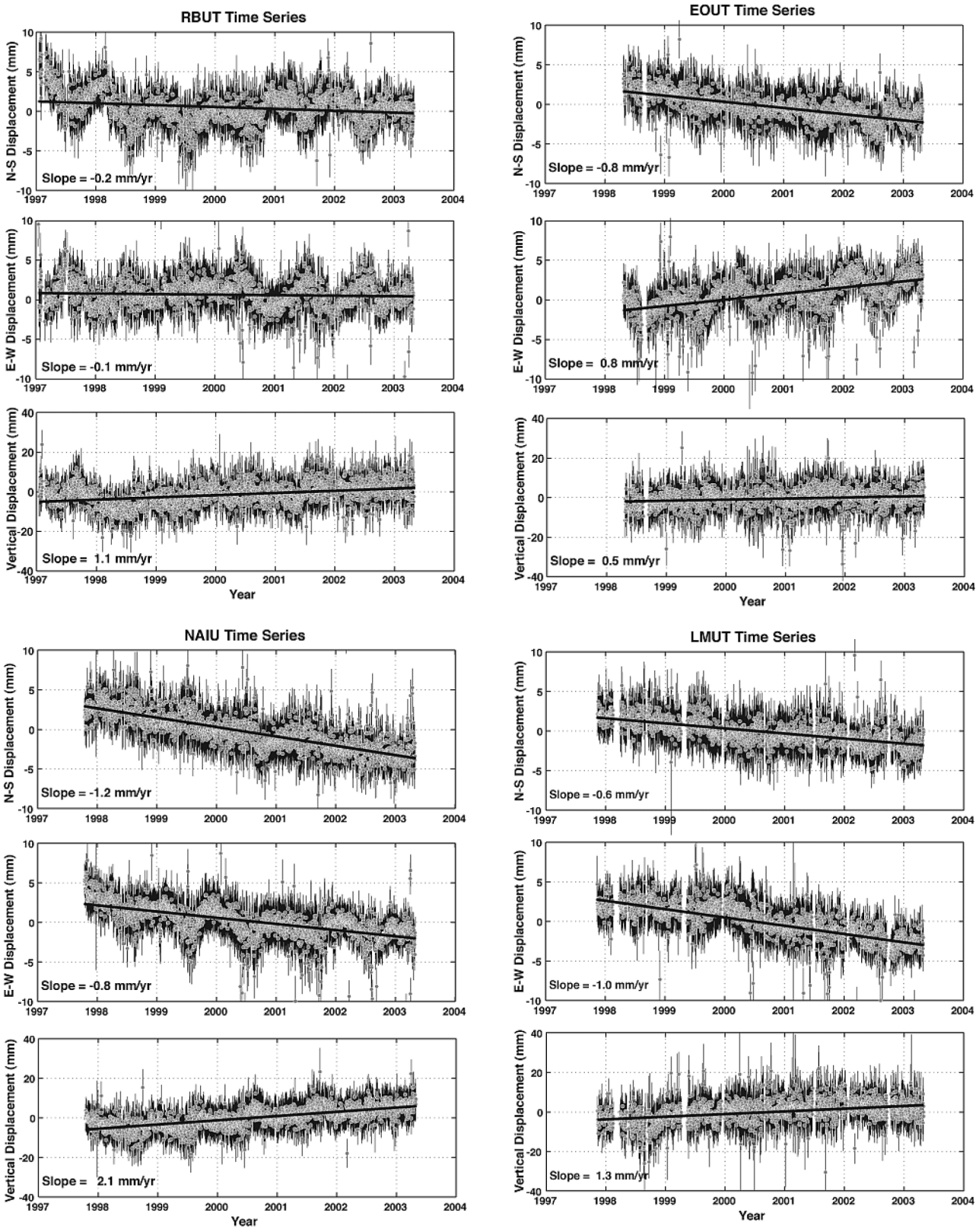

Figure 4. Time series of three-component (N-S, E-W, and vertical) coordinate residuals of four University of Utah continuous GPS stations operated on the Wasatch fault area. Daily data (gray circles) are plotted with 1σ error bars (thin black lines) and fitted linearly by thick black lines. The ITRF velocities were removed from the time series. Negative slopes of the three components represent the southward, westward, and downward motions, respectively.

Table 1. Wasatch Front GPS Velocities in a Stable North America Reference Frame

			Horizontal Velocity and Error, mm/yr						
Station	Longitude	Latitude	V_E	V_N	σ_E	σ_N	θ[a]	V_V	σ_V
				Continuous GPS					
RBUT	−111.809	40.781	−0.43	0.46	0.39	0.29	186.12	1.1	2.5
NAIU	−112.230	41.016	−0.88	−0.49	0.44	0.34	185.16	2.1	2.8
EOUT	−111.929	41.253	0.41	−0.28	0.55	0.42	169.20	0.6	3.5
LMUT	−111.928	40.261	−1.67	−0.03	0.49	0.39	180.37	1.3	3.2
HEBE	−111.373	40.514	0.06	0.09	0.42	0.34	180.09	1.1	2.8
COON	−112.121	40.653	−1.62	−0.38	0.44	0.34	181.15	0.3	3.3
CEDA	−112.861	40.681	−2.28	−0.45	0.39	0.29	182.63	0.7	2.4
CAST	−110.677	39.191	0.53	0.49	0.47	0.36	181.28	−0.2	3.2
SMEL	−112.845	39.426	−1.83	−0.18	0.39	0.31	180.77	−0.2	2.6
				Campaign GPS					
SIDE	−112.148	41.795	−2.06	−0.18	0.67	0.48	192.72		
WEST	−112.063	40.565	−2.66	2.41	0.72	0.58	194.57		
CURV	−112.003	41.757	−1.19	−1.28	0.72	0.53	196.90		
ABRA	−112.110	41.111	−0.58	0.13	0.67	0.53	198.37		
BLMB	−111.951	40.720	−1.26	0.49	0.58	0.43	197.90		
ERDA	−112.253	40.635	−0.87	−0.21	0.72	0.58	193.30		
KIMB	−111.538	40.741	0.16	0.16	0.67	0.53	193.55		
WELL	−111.909	41.651	−2.11	1.89	0.91	0.62	192.15		
3S3E	−111.621	40.584	−0.07	0.13	0.67	0.53	196.52		
BENN	−112.235	41.042	−1.00	0.60	0.67	0.53	199.71		
HOWE	−112.544	41.794	−2.40	−1.09	0.77	0.53	198.72		
MONT	−111.518	41.422	1.23	−0.73	0.72	0.58	181.25		
1S2E	−111.717	40.752	−0.58	0.25	0.67	0.53	193.72		
BEAR	−111.421	41.934	−0.79	1.32	0.53	0.43	186.17		
BAIR	−112.064	41.539	−1.84	−0.13	0.82	0.58	186.59		
BOUN	−111.818	40.964	1.50	0.36	0.67	0.53	195.17		
FRPK	−111.852	41.082	0.27	0.12	0.72	0.53	193.65		
GRA2	−111.818	40.573	0.84	1.02	0.72	0.58	196.16		
LAKE	−112.254	40.702	−0.76	0.71	0.72	0.58	196.55		
QUI2	−111.790	39.940	−0.21	1.31	0.77	0.58	195.90		
KERR	−112.133	40.708	−0.87	0.40	0.67	0.53	198.98		
WILL	−112.007	40.435	−1.97	0.55	0.67	0.53	195.64		
V175	−112.409	40.337	−2.92	−0.17	0.72	0.62	198.22		
0H64	−111.949	40.162	−2.48	1.11	0.67	0.53	192.70		
ELBE	−111.950	39.952	−2.57	1.26	0.72	0.53	185.80		
MONA	−111.853	39.807	−1.15	0.63	0.67	0.58	186.62		
MRPH	−111.930	40.435	−0.86	−0.34	0.67	0.53	195.30		
POLE	−111.538	40.028	−1.07	−0.25	0.82	0.62	202.20		
CAPS	−112.047	39.662	−1.69	1.40	0.77	0.58	175.03		
FERN	−112.104	39.762	−2.34	0.39	0.91	0.67	172.76		
FOOT	−111.746	39.744	0.05	1.25	1.01	0.67	186.44		
H100	−111.020	39.293	−0.52	0.33	1.15	0.67	199.52		
G200	−112.242	39.140	−1.95	−0.19	1.01	0.67	176.59		
MUHA	−112.023	40.727	−1.92	0.38	0.82	0.62	201.42		
FLOR	−112.027	40.588	−1.65	1.42	0.67	0.58	196.68		
HIGH	−111.804	40.653	−1.25	1.70	0.82	0.67	187.94		
RIVE	−111.910	40.531	0.18	1.06	0.86	0.67	191.53		
				IGS Stations[b]					
DRAO	−119.625	49.323	1.83	2.06					−0.61
MDO1	−104.015	30.680	−0.19	0.74					3.12
NLIB	−91.575	41.772	0.02	0.48					1.75
PIE1	−108.119	34.301	−0.03	−0.65					0.46
QUIN	−120.944	39.975	−7.26	8.43					−2.61
GOLD	−116.889	35.425	−4.65	7.33					−0.84
ALBH	−123.487	48.390	5.96	5.16					0.07

[a]The parameter θ is the counterclockwise angle (in degree) from east to the major axis of horizontal error ellipse.
[b]Velocities of these seven IGS stations were used to define the motion of a stable North American reference frame adopted by this study.

[39] Table 1 lists the three components of the derived velocities and their scaled errors of the Wasatch continuous and campaign sites. Figure 5 displays horizontal velocity vectors with error ellipses representing the 95% confident intervals. Note that the vertical velocities have uncertainties greater than 4 to 5 mm/yr for most campaign GPS sites, so that only those velocities determined from continuous GPS were listed in Table 1.

[40] The continuous GPS station velocities show that the hanging-wall sites of the Wasatch fault moved to the west

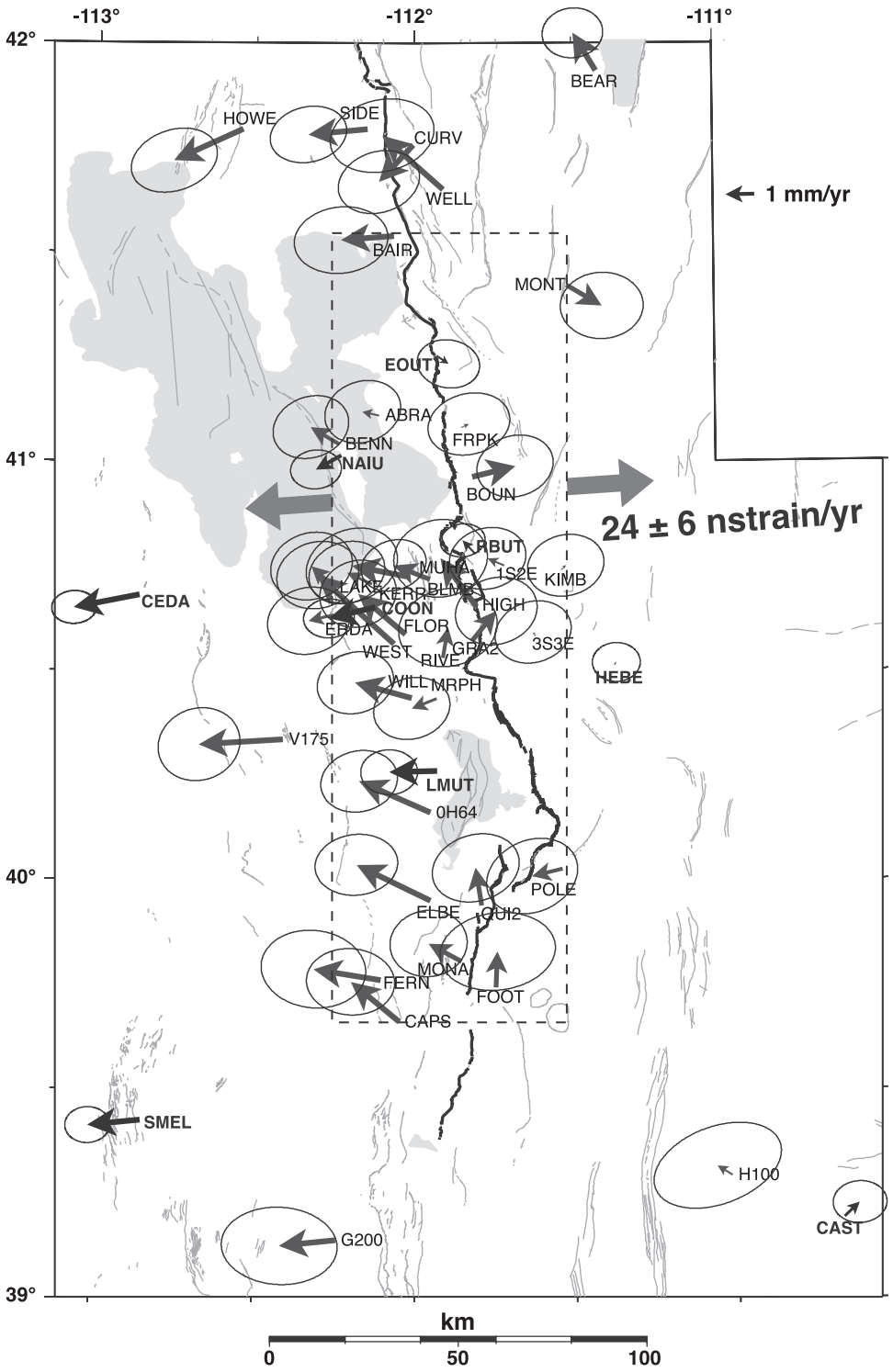

Figure 5. Horizontal velocity vectors, in a stable North America reference frame, derived from the 1997–2004 continuous and the University of Utah 1992–2003 campaign GPS observations. Weighted error ellipses (see text) represent the 95% confident intervals. Gray lines are Quaternary faults, and black lines highlight the Wasatch fault. Thick gray arrows represent the direction of the principal extension assuming a homogeneous strain field in the dashed box.

relative to the footwall sites with velocities increasing westward to 2.3 mm/yr. These data demonstrate an east-west extensional deformation across the entire Wasatch fault zone. In addition, our campaign GPS results reveal nearly east-west motions at most of the sites in the central Wasatch, which are consistent with that determined by continuous GPS. To the north and south, on the other hand, most campaign sites were surveyed only twice (1993 and 2001 for the north; 1994 and 1999 for the south) and their velocity results were not included due to larger errors. Some

Table 2. Wasatch Front Geodetic Strain and Displacement Rates

Measurement	Principal Strain Rate, μstrain/yr		Horizontal Displacement Rate, mm/yr	Azimuth of Least Principal Axis
	Least	Greatest		
This study-1992–2003 campaign GPS	24 ± 6	−7 ± 4	1.6 ± 0.4 (65 km)	86° ± 7°
1992–1995 campaign GPS[a]	49 ± 23	−33 ± 20	2.7 ± 1.3 (55 km)	59° ± 15°
1992–2002 southern Wasatch campaign GPS[b]	24 ± 9	−15 ± 8	1.4 ± 0.5 (60 km)	−77° ± 10°
1972–1990 trilateration[c]	40 ± 10		2.2 ± 0.6 (55 km)	85° ± 5°
1962–1963 triangulation and 1973–1974 trilateration[d]	80 ± 30		2.4 ± 0.9 (30 km)	114° ± 15°

[a]*Martinez et al.* [1998].
[b]*Hammond and Thatcher* [2004].
[c]*Savage et al.* [1992].
[d]*Snay et al.* [1984].

continuous GPS stations recently installed by the University of Utah and the EarthScope, Plate Boundary Observatory project across the northern and southern Wasatch fault, for example, will give better constrains on the deformation rate of the areas.

4.2. Horizontal Strain-Rate Estimates

[41] The horizontal velocities in Figure 5 provide estimates of the contemporary ground motions across the Wasatch fault. Strain rate, defined as relative velocity normalized by distance between two GPS sites, can otherwise reveal how the strain energy in Earth's crust changes with time. The spatial variation of strain rate can show in situ strain concentration that is directly related to local stress concentration and in turn can be used to asses seismic hazard potential [*Ward*, 1994].

[42] This study employed strain rate with the unit of yr^{-1} that is equivalent to 3.2×10^{-8} s^{-1}. The unit of nstrain/yr equals to 10^{-9} yr^{-1} and corresponds to an elongation (positive in sign) or shortening (negative in sign) of 1 mm per 1000 km per year.

4.2.1. Homogeneous Strain Rate Analysis

[43] We employed two independent methods to determine the strain-rate field of the Wasatch area. The first is the DYNAP (Dynamic Adjustment Program) algorithm, designed to estimate six crustal kinematic parameters from geodetic data such as three-dimensional relative displacement vectors obtained from GPS or VLBI [*Drew and Snay*, 1989]. These crustal dynamic parameters were then used to compute the four elements of the matrix of horizontal deformation rate and the two components of the vertical tilt rate vector. Note that the DYNAP method assumes a spatially and temporally homogeneous strain field, thus the result is considered as a first-order estimate of the strain rate without taking into account spatial strain variation. To solve for spatial distribution of the strain-rate field, the second method of a weighted least-squares inversion will be discussed in section 4.2.2.

[44] Figure 5 shows the direction and magnitude of the least-principal (or maximum extensional) strain rate across the Wasatch fault. Table 2 lists these results along with the rates from other studies. Our campaign GPS observations were collected in a longer time period, 1992–2003, and thus provide a higher precision on strain-rate measurement than that from *Savage et al.* [1992] and *Martinez et al.* [1998]. The principal extensional rate of 24 ± 6 nstrain/yr, oriented nearly E-W, corresponds to a relative west motion of 1.6 ± 0.4 mm/yr across the 65 km-wide network and agrees with other geodetic results listed in Table 2 within the 95% confidence interval.

[45] Note in Table 2 that the minimum extensional (or the greatest-principal) strain rate of −7 ± 4 nstrain/yr, a factor of 3.4 smaller than the maximum extensional rate, is not significant to a confidence level of 95%. Therefore the uniform strain field across the Wasatch fault area is best characterized as uniaxial extension. The campaign GPS data of *Hammond and Thatcher* [2004] also revealed uniaxial extension south of 39.5°N across the southern Wasatch fault (groups 6 and 7 in Table 3 of their paper).

[46] Homogeneous strain rates to the east and west of the Wasatch fault were evaluated to better understand how the regional deformation is distributed across the fault. To the east of the fault, data from 16 GPS stations on the footwall block (Figure 3) reveal a principal extensional rate of 5 ± 10 nstrain/yr oriented nearly E-W. This rate is equivalent to zero to a confidence level of 95%, indicating that the Wasatch footwall, tectonically the Rocky Mountains, has not been deformed significantly during the period of our GPS observations.

[47] The deformation of the hanging-wall block was determined using GPS data from 25 stations west of the Wasatch fault (Figure 3). The result reveals a principal extensional strain rate of 22 ± 27 nstrain/yr, and the statistic t-test indicates that this rate is, within a significance level of 95%, higher than 5 ± 10 nstrain/yr of the footwall and equivalent to 24 ± 6 nstrain/yr across the fault.

[48] Further west of the Wasatch fault zone, our GPS data provided poor constrains on determining the far-field strain field mainly due to the sparse distribution of stations west of ~112.3°W (Figure 3), thus the comparison of strain rates between the Wasatch fault area and the eastern Basin-Range is not statistically meaningful. However, many regional GPS studies suggested that the strain rate decreases from the Wasatch fault to the west into the eastern Basin-Range. For example, *Hammond and Thatcher* [2004] indicated a maximum extensional strain rate of 13.3 ± 8.3 nstrain/yr between 112.7°W and 111.9°W near 39°N, which is smaller than our Wasatch rate of 24 ± 6 nstrain/yr within a significance level of 95%. *Bennett et al.* [2003] also estimated a strain rate of 7 ± 3 nstrain/yr over a region of ~200 km wide across the eastern Basin-Range.

[49] In summary, the above homogeneous strain analysis reveals that there is an abrupt transition in extensional deformation from east to west across the Wasatch fault into the eastern Basin-Range. While the footwall block remains un-deformed, the extensional strain rate increases sharply to

24 ± 6 nstrain/yr in the hanging-wall near the fault and then decreases to ~10 nstrain/yr in the eastern Basin-Range, which suggests a concentration of crustal strain accumulation along the Wasatch fault between the eastern Basin-Range and the Rocky Mountains.

4.2.2. Spatial Variation of Strain Rates

[50] Before employing the second method, we used a simple analysis of one-dimensional strain variation based on the lateral change of the westward motions across the Salt Lake City segment of the central Wasatch fault (Figure 6a). We selected this area because the distribution of the GPS stations is denser than that across the northern and southern parts of the fault. In Figure 6b, a strain rate of 30 ± 8 nstrain/yr was determined by a weighted least-squares estimate of the west velocities of all 14 GPS stations. This value is similar to 24 ± 6 nstrain/yr determined from DYNAP, as was expected because both results are under the assumption of constant strain rate field.

[51] Applying the same analysis to different zones of the area, however, reveals that the east-west strain rate is larger, within a significance level of 95% according to the t-test, in the hanging-wall of the Wasatch fault (Figures 6d and 6e) than in the footwall (Figure 6c). In addition, the west velocities tend to increase notably from the fault to the west (Figure 6e) and then decrease, implying that high strain rate, or strain concentration, occurs in the hanging-wall zone adjacent to the Wasatch fault. This implication also agrees with that from the homogeneous strain analysis in section 4.2.1.

[52] We further evaluated the two-dimensional variation of strain rate of the whole Wasatch area by employing an algorithm of weighted least-squares inversion that uses station velocities to solve for strain-rate components [*Shen et al.*, 1996]. Unlike the DYNAP algorithm, which assumes a spatially uniform strain field, this method determines strain rates as continuous function in space within the entire GPS network.

[53] Figure 7a shows grid values of horizontal strain rates in the Wasatch area, with a distance-decaying constant σ_D of 50 km. This constant defines how an observed velocity value d km away from a grid is weighted by a factor of $\exp(-d/\sigma_D)$ in the strain rate estimation of that grid (see Appendix for the mathematic definition). Contours in Figure 7a reveal the distribution of maximum extensional strain rates. Note that the errors are more than a factor of two larger than the DYNAP results because data from distant stations have smaller weights; i.e., this method effectively uses fewer observations to estimate strain rate for each grid. The best results, with errors of 20 nstrain/yr or less, indicate extensional strain rates of ~30 nstrain/yr across the central Wasatch fault. Within the 95% confident interval, these rates agree with the values determined by the DYNAP algorithm (Figure 5) and the linear regression of west velocities (Figure 6b) assuming a uniform strain-rate field across the Wasatch fault.

[54] Figure 7b, on the other hand, shows a strain-rate model with σ_D = 30 km that revealed spatial variations of the regional strain field in more detail. The overall errors, however, are about a factor of two higher than the model of σ_D = 50 km; therefore we only focused on the central Wasatch fault area (dashed box in Figure 7b) where a denser distribution of GPS station provides relatively better spatial resolution for the strain rate estimates.

[55] Figure 7c shows that the principal extensional strain rates are 30 to 42 nstrain/yr in a 25 km-wide zone across the central Wasatch fault, with the values decreasing westward to ~10 nstrain/yr near the Oquirrh fault. Despite the large uncertainties, ~30–40 nstrain/yr associated with the contours, the lateral variation of strain rate shown in Figure 7c is supported by the previous homogeneous strain analysis and least-squares fits of GPS west velocities (Figure 6), implying that the crustal deformation in the Wasatch region is mainly close to the Wasatch fault instead of being distributed evenly across the area.

[56] Figures 7a and 7b also reveal possible north-south variations of extensional strain rate in the Wasatch fault area: the rates seem to be larger at the northern and southern ends of the network. Likewise, this scenario cannot be justified statistically because of the large uncertainties, mostly ≥40 nstrain/yr, in both models. Homogeneous strain analysis for these two parts of the network also introduced large errors mainly because most campaign sites were surveyed only twice to the north (1993 and 2001) and south (1994 and 1999). Therefore, our current GPS data are not able to resolve significant variations of strain rates along the Wasatch fault from north to south.

5. Discussion

[57] Geodetic technologies such as GPS have been used to determine contemporary ground deformation and examine how strain is accumulated in Earth's crust. For normal faults like the Wasatch fault, geologic measurements of net vertical tectonic displacement from fault trenching of Late Quaternary sediments provide an estimate of fault-slip rate over a longer time period. The integration of these two types of data can reveal temporal variations of strain loading and release on faults through earthquake cycles, and thus provide information on the selection of earthquake recurrence models for seismic hazard analysis [e.g., *Friedrich et al.*, 2003; *Malservisi et al.*, 2003].

[58] The conversion between vertical fault-slip rate and horizontal surface-extension rate of a normal fault requires working models of subsurface fault geometry and ground deformation during an earthquake. In Figure 8c, for example, vertical fault displacement, or fault throw t, is related to horizontal fault displacement, or fault heave h, and the horizontal extension, ε, through the trigonometric relation

$$\varepsilon = \mathrm{h} = \mathrm{t}/\tan\theta, \tag{2}$$

where θ is the fault dip. Note that the Wasatch fault was considered to steepen upward (≥70°) near the surface due to fault refraction caused by a lack of confining pressure in unconsolidated deposits [e.g., *Gilbert*, 1928; *McCalpin*, 1996], so here θ represented the dip of subsurface fault plane that remained relatively straight during earthquake rupture (Figures 8c and 8d).

[59] On the basis of equation (2), one can convert vertical displacement rates, $\dot{\mathrm{t}}$, derived from various geologic estimates of fault-slip rate, to horizontal displacement rates, $\dot{\mathrm{h}}$, and then compare them with horizontal extension rates, $\dot{\varepsilon}$, measured by GPS. Accordingly, *Friedrich et al.* [2003]

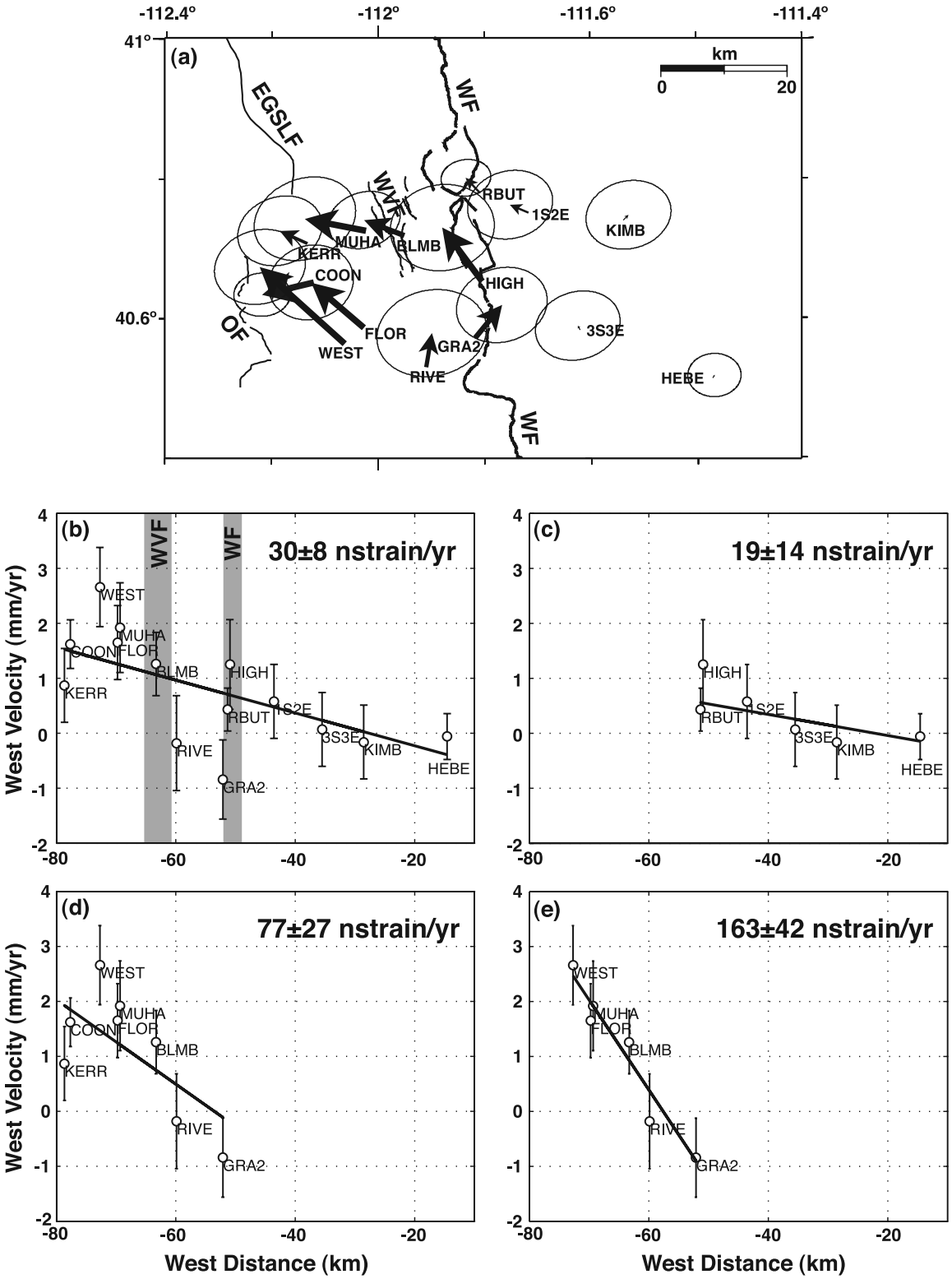

Figure 6. (a) Horizontal GPS velocities near the central Wasatch fault (WF) with 2σ errors. Secondary faults in the area include: WVF, the West Valley fault; OF, the Oquirrh fault; EGSLF, the East Great Salt Lake fault. (b)–(e) Strain rates in the E-W direction determined by weighted least-square fits of west velocities across different zones of the area. Error bars represent 1σ. The hanging-wall of the Wasatch fault (d and e) shows significantly higher strain rates than the footwall (c).

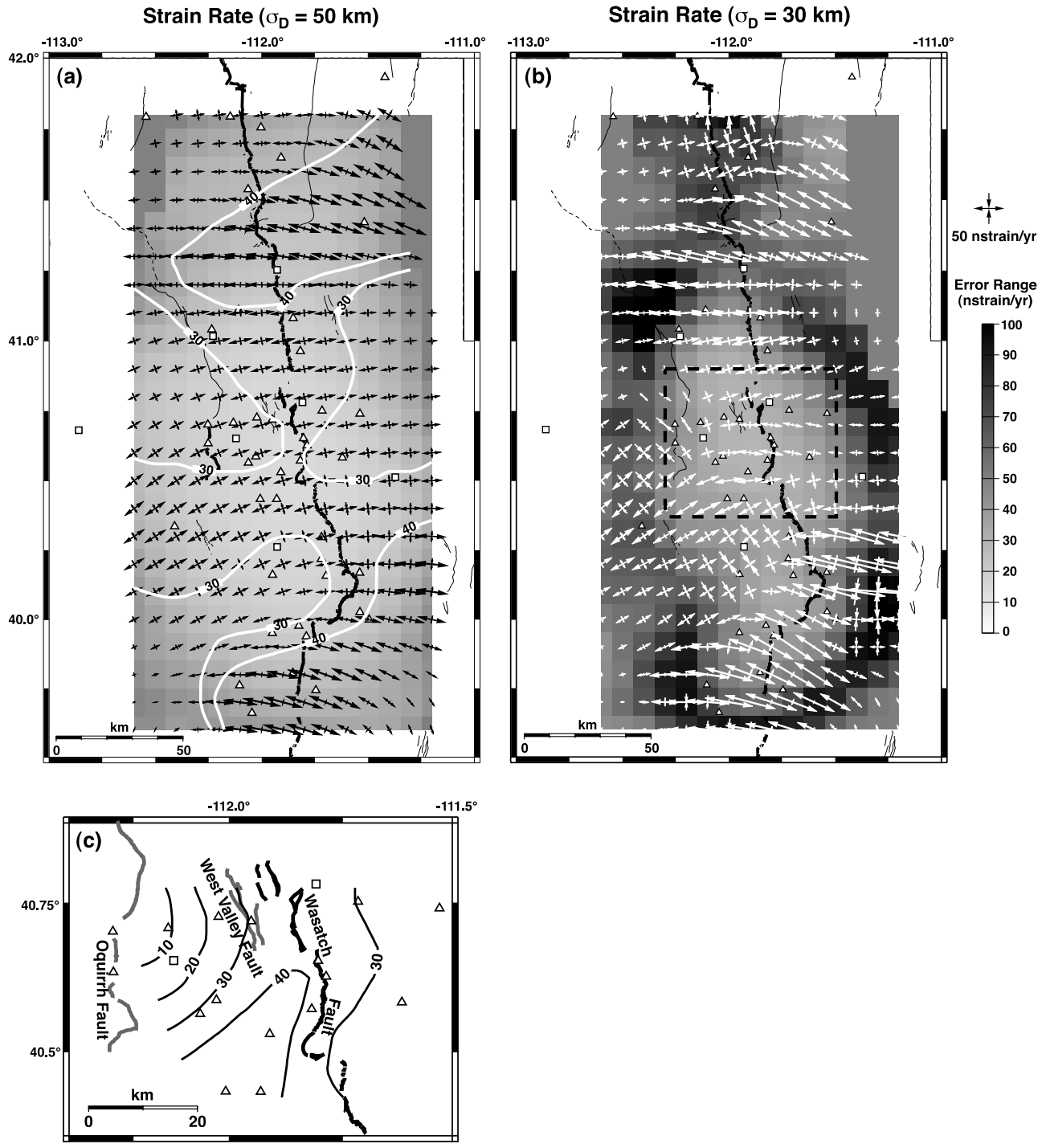

Figure 7. The Wasatch Front horizontal strain-rate field determined by GPS velocities. Grayscale shading represents 1σ error ranges. Rectangles and triangles indicate continuous and campaign GPS sites, respectively. (a) Principal strain rates (black arrows) with σ_D = 50 km (see Appendix). White curves show contours of the maximum extensional rates. (b) Principal strain rates (white arrows) with σ_D = 30 km. (c) Contours of the maximum extensional strain rates across the central Wasatch fault (dashed box in (b)).

calculated the average horizontal displacement rates for the Wasatch fault from Middle Miocene to Holocene and proposed that the rates are higher than the current GPS horizontal extension rates in the hanging-wall if the fault dips shallowly (30°), but are lower if the fault dips steeply (60°). We emphasize, however, that this comparison of the two rates $\dot{h}$ and $\dot{\varepsilon}$ using equation (2) may be misleading due to the more likely nonvertical simple-shear deformation in the hanging-wall during a normal-fault earthquake rupture. This simple-shear deformation model is illustrated in Figure 8 and will be discussed in the following contents.

[60] To determine the detailed relationship between the geometry of a normal fault and of the sediments in its hanging-wall, *White et al.* [1986] developed a finite-strain

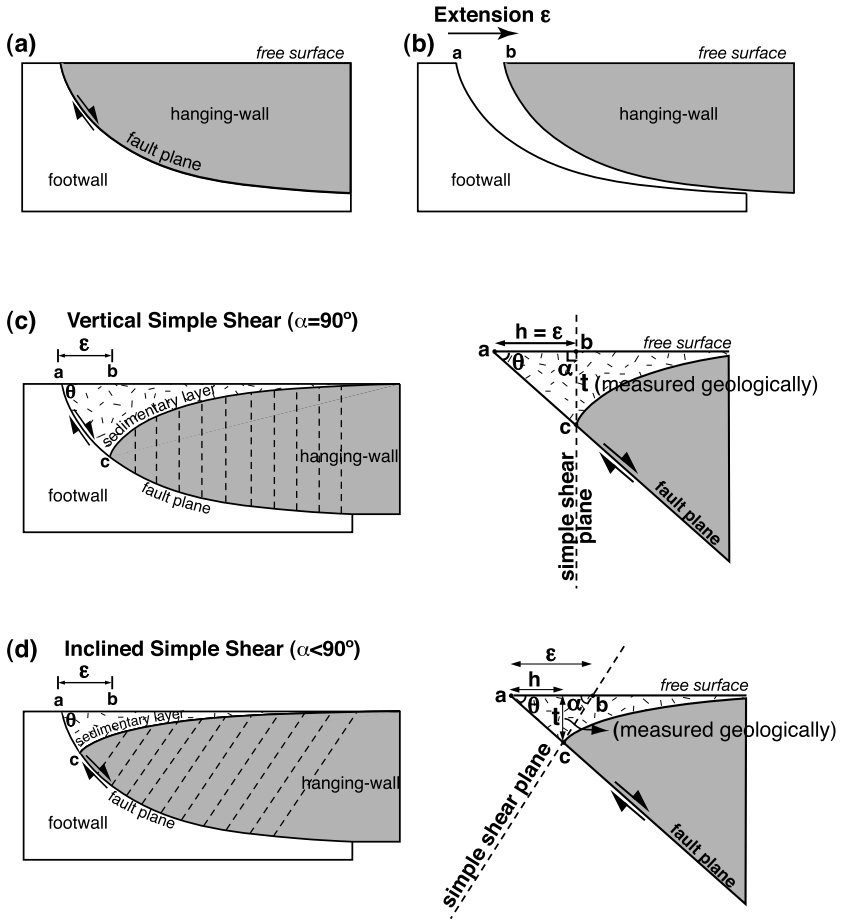

Figure 8. Finite-strain model for normal-fault rupturing [after *White et al.*, 1986]. (a) Before fault rupture. (b)–(d) The hanging-wall extends e relative to the footwall and then deforms by simple shear to fill the potential void beneath it, such that point **a** moves to **b** during the extension and then to **c** during the simple shear. Note that the footwall remains undeformed. The right parts of (c) and (d) illustrate the geometric relation between horizontal extension ε, measured by GPS, and vertical fault displacement **t**, derived from geologic data. θ and α are the dips of the fault and simple-shear plane, respectively, and **h** represents the horizontal fault displacement. (c) $\alpha = 90^\circ$ for a vertical simple shear, so $\varepsilon = \mathbf{h} = \mathbf{t}/\tan\theta$. (d) $\alpha < 90^\circ$ for a inclined simple shear, so $\varepsilon = \mathbf{h} + \mathbf{t}/\tan\alpha$. See text for detailed discussions.

model, i.e. for strain greater than 10^{-6}, in which the hanging-wall is assumed to experience a simple-shear deformation during fault rupture. This assumption implies that the hanging-wall is deformed by motion on many parallel small faults that do not intersect, of the type revealed by seismic reflection profiles in their study or similar to the dashed lines illustrated in Figures 8c and 8d. Based on three seismic sections across normal faults, *White et al.* [1986] also showed that this simple shear did not occur on vertical planes, but on planes inclined toward the fault at $\sim 45^\circ$, so seismic reflectors of fault plane and sedimentary beds can be consistently interpreted. The non-vertical simple shear also agrees with the observation that antithetic faults in hanging-walls are rarely vertical [e.g., *Jackson*, 1987].

[61] Moreover, the study of *White et al.* [1986] demonstrated that the amount of horizontal extension across a normal fault couldn't be estimated simply from the apparent fault offset without the knowledge of the dip of the simple shear planes in the hanging-wall. In Figure 8, the relation between ε and t is

$$\varepsilon = \mathrm{h} + \mathrm{t}/\tan\alpha = \mathrm{t}/\tan\theta + \mathrm{t}/\tan\alpha, \tag{3}$$

where α represents the dip of the simple-shear plane. A special case of $\alpha = 90^\circ$ (Figure 8c) shows that if the simple-shear occurred on a vertical plane, then the fault heave is simply equivalent to the horizontal extension and equation (2) holds.

[62] For nonvertical simple shear (Figure 8d), which is more likely according to *White et al.* [1986], a given amount of horizontal extension would overestimate the true vertical displacement by a factor of $1 + \tan\theta/\tan\alpha$ if equation (2) was applied; for example, a factor of 2.0, 1.5, and 1.3 for a fault dip of 55° and simple-shear inclinations of 55°, 70°, and 80°, respectively (Figure 9b). Therefore, the dips of a normal fault and the associated simple-shear plane are two important parameters for converting horizontal extension,

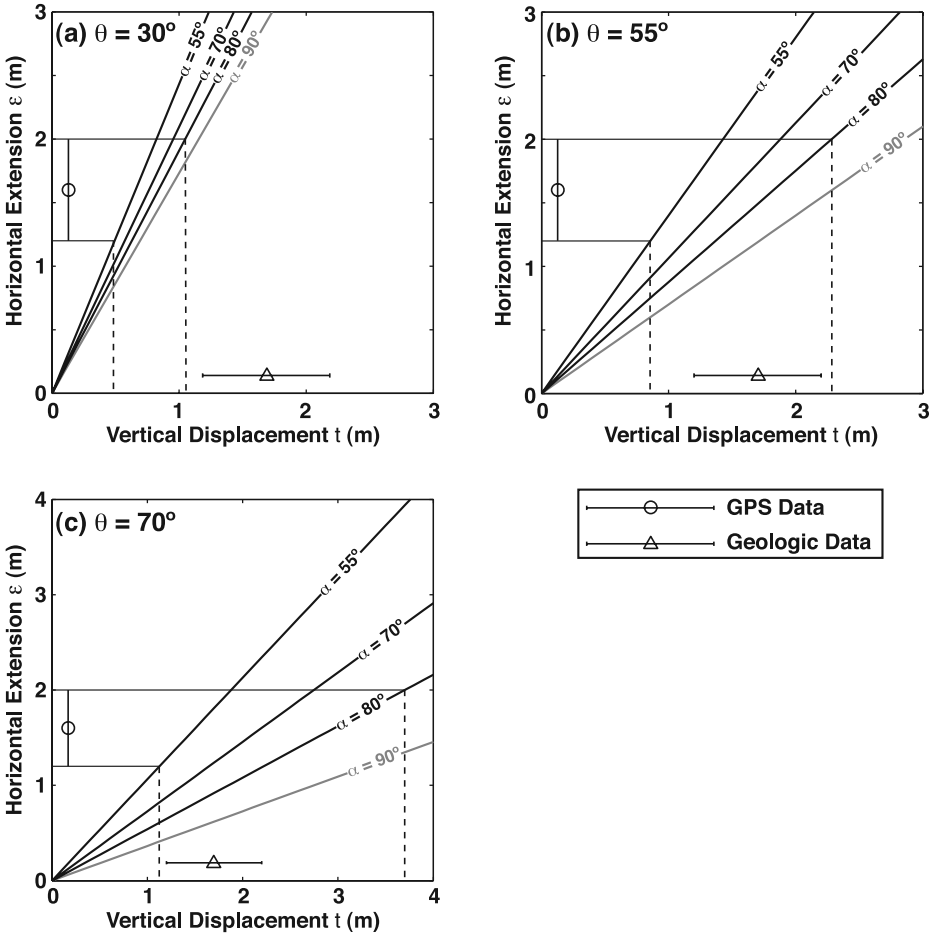

Figure 9. Relationships between vertical fault displacement (t) and horizontal extension (ε) corresponding to different dips of normal fault (θ) and simple-shear (α) planes; i.e. $t = \varepsilon/(1/\tan\theta + 1/\tan\alpha)$ (Figure 8d). Dashed lines in each panel demonstrate the ranges of vertical displacement converted from GPS-measured horizontal extension (circle with 1σ error bar) for plausible values of α for the Wasatch fault. Triangle with 1σ error bar represents the Holocene slip rate of the Wasatch fault [*Friedrich et al.*, 2003].

measured by GPS, to vertical fault displacement. We will next discuss these parameters for the Wasatch fault.

[63] *Zoback* [1983] reported a range of 44° to 70° for dips measured on bedrock scarps and gravity models along segments of the Wasatch and adjacent faults. *Harris et al.* [2000] suggested similar values of 26°–50° from 65 field observations of dip made on fault scarps, fault drag geometry, and the lowest faceted spurs of the central and southern Wasatch fault. Focal mechanisms of large Basin-Range normal-faulting earthquakes, in addition, indicated that co-seismic slips occurred on fault planes dipping 45°–60° [e.g., *Doser and Smith*, 1989]. Based on these observations, *Wong et al.* [2002] proposed the range of the average fault dip from 30° to 70° to the west, with the preferred value of 55°W, for estimating the earthquake ground-shaking hazard of Salt Lake City.

[64] By postulating that the antithetic fault can reasonably represent the shear plane when the hanging-wall deformed during a normal-faulting earthquake, we approximated the simple-shear inclination as the dip of the West Valley fault zone, located 10 km west of the central Wasatch fault near Salt Lake City (Figures 6a and 7c) and assumed to be antithetic to the Wasatch fault [e.g., *Keaton et al.*, 1993]. *Wong et al.* [2002] suggested possible dips of 55°, 70°, and 80° to the east, with the preferred value 70°, for the West Valley fault zone.

[65] Applying equation (3) and assuming a dip of 55°W for the Wasatch fault, our GPS horizontal velocity of 1.6 ± 0.4 mm/yr across the fault (Table 2) is converted to vertical displacement rates of 0.9–2.3 mm/yr and 1.7–2.9 mm/yr for the antithetic fault dipping 55°E–80°E and 90°, respectively (Figure 9b). These vertical rates are consistent, within 1σ errors, with the geologic fault-displacement rates of 1.7 ± 0.5 mm/yr over a period of 0–10 ka ago on the Wasatch fault [*Friedrich et al.*, 2003], implying that the contemporary rate of strain loading agreed with the average Holocene rate of strain release in the brittle part of the crust. This scenario also implies that the Wasatch fault has occurrence rates of large earthquakes similar to that derived from the paleoearthquake records in the past 10 ka.

[66] While the above results are based on a preferred dip for the Wasatch fault (55°W), two end-member working

Table 3. Comparison of Deformation Rates Across the Wasatch Fault From GPS and Geologic Determinations

Dip of the Wasatch Fault	Dip of Simple Shear Plane (Antithetic Fault)	Vertical Displacement Rate from GPS Data,[a] mm/yr	Geologic Fault Slip Rate (0–10 ka),[b] mm/yr	Comparison of GPS Rate with Geologic Rate[c]
$\theta = 30°$	$\alpha = 55°E–80°E$	0.5–1.0	1.7 ± 0.5	GPS < Geologic
	$\alpha = 90°$	0.7–1.2	1.7 ± 0.5	GPS < Geologic
$\theta = 55°$	$\alpha = 55°E–80°E$	0.9–2.3	1.7 ± 0.5	Consistent
	$\alpha = 90°$	1.7–2.9	1.7 ± 0.5	Consistent
$\theta = 70°$	$\alpha = 55°E–80°E$	1.1–3.7	1.7 ± 0.5	Consistent
	$\alpha = 90°$	3.3–5.5	1.7 ± 0.5	GPS > Geologic

[a]Vertical displacement rates were converted from the GPS-derived horizontal extension rates across the Wasatch fault, 1.6 ± 0.4 mm/yr, using equation (3).
[b]Holocene (0–10 ka) geologic slip rates of 1.7 ± 0.5 mm/yr for the Wasatch fault were determined by *Friedrich et al.* [2003].
[c]Comparison of the two rates was based on 1σ error ranges.

models for subsurface fault geometry are worth noting. First, for a shallow fault dip of 30°W, the GPS extension rate corresponds to vertical displacement rates of 0.5–1.0 mm/yr and 0.7–1.2 mm/yr for the antithetic fault dipping 55°E–80°E and 90°, respectively, lower than the geologic rates of 1.7 ± 0.5 mm/yr (Figure 9a). The shallowly dipping (≤30°W) Wasatch fault thus implies a lower rate of contemporary strain loading than the average Holocene strain release, namely the fault could have lower earthquake occurrence rate at present time or the earthquakes had been clustered over the past 10 kyr.

[67] For a working model with steeper fault dip, $\theta = 70°$W, on the other hand, the GPS rate corresponds to vertical rates of 1.1–3.7 mm/yr for $\alpha = 55°E–80°E$. The Holocene fault displacement rate of 1.7 ± 0.5 mm/yr is within this interval at the lower end (Figure 9c), indicating consistency between the geologic and GPS rates. For $\alpha = 90°$, however, the GPS rate corresponds to vertical rate of 3.3–5.5 mm/yr that is higher than the geologic rates. Models with steep fault dip (>∼60°W) and vertical simple-shear plane thus implies higher rates for contemporary strain loading than the average Holocene strain release.

[68] Table 3 summarizes the above discussions, suggesting that the comparison between the GPS and geologic rates for the Wasatch fault depends on model assumptions of subsurface fault geometry and the process of normal-fault rupturing. Although our preferred model, with the fault dipping 55°W and simple-shear planes dipping 55°E–80°E, indicated consistent rates between the contemporary strain loading from GPS data and the average strain release in the past 10 ka from geologic data, other plausible fault models showed that the two rates can be different within the uncertainties of fault dips and strain-rate measurements.

[69] Determining fault-slip rate from geodetic observations also requires incorporating earthquake deformation cycle, in which Earth's crust deforms at different rates in different stages between two earthquakes [e.g., *Thatcher*, 1983]. For the Wasatch fault, *Malservisi et al.* [2003] employed finite element models with elastic upper crust and viscoelastic lower crust/upper mantle to estimate the present ground motion caused by an earthquake occurred 1200 years ago. Results that best fit the geodetic data of seven continuous GPS stations across the eastern Basin-Range suggested that modeled rates of horizontal extension are in agreement with the Holocene fault-slip rates. Therefore, although beyond the scope of this study, earthquake cycle effects such as post-seismic relaxation need to be evaluated for modeling inter-seismic fault-slip rate from the contemporary geodetic observations of the Wasatch fault [e.g., *Chang and Smith*, 2004].

6. Conclusions

[70] This study provides a comprehensive evaluation on the contemporary ground deformation of the Wasatch fault, Utah, using GPS measurements and accesses the overall kinematics of the eastern Basin-Range province. The Wasatch campaign and continuous GPS data were analyzed together to provide estimates of velocity and strain-rate fields along the fault. Results assuming homogeneous stain field revealed an east-west extensional strain rate of 24 ± 6 nstrain/yr that corresponds to a horizontal ground motion of 1.6 ± 0.4 mm/yr across a 65 km-wide zone encompassing the Wasatch fault. This motion accommodates ∼50% of the crustal deformation across the 200 km-wide eastern Basin-Range, which is ∼3 mm/yr as determined by continuous GPS and VLBI. Interpolating the velocity field from our GPS data, on the other hand, revealed the variation of extensional strain rates from 30 to 42 nstrain/yr over a 25 km-wide zone at the central Wasatch fault. These rates are larger than the average value of 24 ± 6 nstrain/yr, suggesting that the crustal strain accumulation between the eastern Basin-Range and the Rocky Mountains is concentrated along the Wasatch fault. We employed a simple-shear rupture model for the Wasatch fault, by which the contemporary, GPS-determined, horizontal deformation rates were compared with the Holocene, geologically derived, fault displacement rates. Our results suggested that the comparison between the two rates strongly depends on models of subsurface fault geometry that are not constrained by subsurface data such as seismic reflection surveys, and the process of normal-fault rupturing. A working model with the antithetic fault, which represent the simple-shear planes, dipping 55°E–80°E implied that the Wasatch fault would have lower rates of the contemporary strain loading than the average Holocene (0–10 ka) strain release if the fault dips shallowly (≤30°W). These two estimates of strain rates are consistent within their 1σ error ranges, however, if the fault dips steeper (>30°W).

Appendix A

[71] The strain-rate modeling method of *Shen et al.* [1996] employed a weighted least-squares inversion using station velocities and their covariances to solve for strain

rate components. The weighting factor is calculated by a Gaussian window

$$E_{ij} = C_{ij} \exp\left(\frac{R_I^2 + R_J^2}{\sigma_D^2}\right), \quad \text{(A1)}$$

where i and j are the velocity components corresponding to the Ith and Jth stations, R_I and R_J the distances to the point to be estimated, and σ_D is a distance-decaying constant. For example, $\sigma_D = 50$ km corresponds to a spatial smoothing by a Gaussian window with one standard deviation of 50 km centered at the point where strain rate is estimated. This window weighs data 50% for sites 42 km from the center. For σ_D = 30 km, in comparison, the distance of 50% weighting is decreased to 25 km.

[72] **Acknowledgments.** This project has been a long-term, multi-institutional project of the University of Utah Seismology and Active Tectonics research group. We appreciate the efforts of David Drobeck, Ken Whipp, and Terry Dye for installing and maintaining the Wasatch Front GPS stations and telemetry system and to Dan Trentman for help with computational needs. We thank Teresa Van Hove of UCAR for assisting GPS data recording and automatic processing. We particularly note that the field projects were greatly benefited by the assistance of undergraduate and graduate students of the University of Utah and Brigham Young University. UNAVCO (University Navstar Consortium) is thanked for technical support and data archiving. Also we thank the staff from the Utah Geological Survey and of the Bureau of Land Management who assisted in our early field efforts. The county surveyors of Salt Lake, Utah, Weber, and Cache counties, Utah, provided related GPS network support. We note that the collaborative exchange of data between this project and BARGEN (Basin and Range Geodetic Network) helped expand the GPS spatial coverage of this project. Comments from Tim Dixon, Bill Hammond, and Wayne Thatcher greatly benefited this paper. This research was funded by the U.S. Geological Survey NEHRP (National Earthquake Hazard Reduction Program) grants 02HQGR0098 and 04HQAG0023, by the NSF Continental Dynamics project grant EAR0314237, and by internal University of Utah support.

References

Agnew, D. C. (1992), The time-domain behavior of power-law noise, *Geophys. Res. Lett.*, *19*, 333–336.

Arabasz, W. J., J. C. Pechmann, and E. D. Brown (1992), Observational seismology and the evaluation of earthquake hazards and risk in the Wasatch Front area, Utah, in *Assessment of Regional Earthquake Hazards and Risk Along the Wasatch Front, Utah*, edited by P. L. Gori and W. W. Hays, *U. S. Geol. Surv. Prof. Pap.*, *1500-A-J*, D1–D36.

Bawden, G. W., W. Thatcher, R. S. Stein, K. W. Hudunt, and G. Peltzer (2001), Tectonic contraction across Los Angles after removal of groundwater pumping effects, *Nature*, *412*, 812–815.

Bennett, R. A., B. P. Wernicke, N. A. Niemi, A. M. Friedrich, and J. L. Davis (2003), Contemporary strain rates in the northern Basin and Range province from GPS data, *Tectonics*, *22*(2), 1008, doi:10.1029/2001TC001355.

Blewitt, G., and D. Lavallée (2002), Effect of annual signals on geodetic velocity, *J. Geophys. Res.*, *107*(B7), 2145, doi:10.1029/2001JB000570.

Blewitt, G., D. Lavallée, P. Clarke, and K. Nurutdinov (2001), A new global mode of Earth deformation: Seasonal cycle detected, *Science*, *294*, 2342–2345.

Brockmann, E. (1996), Combination of solutions for geodetic and geodynamic applications of the Global Positioning System (GPS), Ph.D. dissertation, 211 pp., Astron. Inst., Univ. of Berne, Berne, Switzerland.

Chang, W. L., and R. B. Smith (2002), Integrated seismic-hazard analysis of the Wasatch Front, Utah, *Bull. Seismol. Soc. Am.*, *92*, 1904–1922.

Chang, W. L., and R. B. Smith (2004), Postseismic and interseismic deformation of large normal-faulting earthquakes in the Basin-Range, *Eos. Trans. AGU*, *85*(47), Fall Meet. Suppl., Abstract G13A-0797.

Davis, J. L., R. A. Bennett, and B. P. Wernicke (2003), Assessment of GPS velocity accuracy for the Basin and Range Geodetic Network (BARGEN), *Geophys. Res. Lett.*, *30*(7), 1411, doi:10.1029/2003GL016961.

Dixon, T. H., M. Miller, F. Farina, H. Wang, and D. Johnson (2000), Present-day motion of the Sierra Nevada block and some tectonic implication for the Basin and Range province, North America Cordillera, *Tectonics*, *19*, 1–24.

Doser, D. I., and R. B. Smith (1989), An assessment of source parameters of earthquakes in the cordillera of the western United States, *Bull. Seismol. Soc. Am.*, *79*, 1383–1409.

Drew, A. R., and R. A. Snay (1989), DYNAP: Software for estimating crustal deformation from geodetic data, *Tectonophysics*, *162*, 331–343.

Eddington, P. K., R. B. Smith, and C. Renggli (1987), Kinematic of Basin and Range intraplate extension, in *Continental Extensional Tectonics*, edited by M. P. Coward et al., *Spec. Publ. Geol. Soc.*, *28*, 371–392.

Friedrich, A. M., B. P. Wernicke, N. A. Niemi, R. A. Bennett, and J. L. Davis (2003), Comparison of geodetic and geologic data from the Wasatch region, Utah, and implications for the spectral character of Earth deformation at periods of 10 to 10 million years, *J. Geophys. Res.*, *108*(B4), 2199, doi:10.1029/2001JB000682.

Gilbert, G. K. (1928), Studies of Basin Range structure, *U.S. Geol. Surv. Prof. Pap.*, *153*, 1–92.

Hammond, W. C., and W. Thatcher (2004), Contemporary tectonic deformation of the Basin and Range province, western United States: 10 years of observation with the Global Positioning System, *J. Geophys. Res.*, *109*, B08403, doi:10.1029/2003JB002746.

Harris, R. A., R. B. Smith, W. L. Chang, C. M. Meertens, and A. M. Friedrich (2000), Temporal distribution of extensional strain across the southern Wasatch fault zone: Geological constraints for the GPS velocity field, *Eos. Trans. AGU*, *81*(48), Abstract T22A-08.

Hecker, S. (1993), Quaternary tectonics of Utah with emphasis on earthquake-hazard characterization, *Utah Geol. Surv. Bull.*, *127*, 157 pp., 2 plates.

Hugentobler, U., S. Schaer, and P. Fridez (2001), Bernese GPS software version 4.2, 511 pp., Astron. Inst., Univ. of Berne, Berne, Switzerland.

Jackson, J. A. (1987), Active normal faulting and crustal extension, in *Continental Extensional Tectonics*, edited by M. P. Coward, J. F. Dewey, and P. L. Hancock, *Spec. Publ. Geol. Soc.*, *28*, 3–17.

Keaton, J. R., D. R. Currey, and S. J. Olig (1993), Paleoseismicity and earthquake hazards evaluation of the West Valley fault zone, Salt Lake City urban area, *Contract Report 93-8*, 55 pp., Utah Geol. Surv., Salt Lake City.

Machette, M. N., S. F. Personius, and A. R. Nelson (1992), Paleoseismology of the Wasatch fault zone: A summary of recent investigations, interpretations, and conclusions, in *Assessment of Regional Earthquake Hazards and Risk Along the Wasatch Front, Utah*, edited by P. L. Gori and W. W. Hays, *U. S. Geol. Surv. Prof. Pap., 1500-A-J*, A1–A71.

Malservisi, R., T. H. Dixon, P. C. La Femina, and K. P. Furlong (2003), Holocene slip rate of the Wasatch fault zone, Utah, from geodetic data: Earthquake cycle effects, *Geophys. Res. Lett.*, *30*(13), 1673, doi:10.1029/2003GL017408.

Mao, A., C. G. A. Harrison, and T. H. Dixon (1999), Noise in GPS coordinate time series, *J. Geophys. Res.*, *104*, 2797–2816.

Martinez, L., C. M. Meertens, and R. B. Smith (1998), Rapid deformation rates along the Wasatch fault zone, Utah, from first GPS measurements with implications for earthquake hazard, *Geophys. Res. Lett.*, *25*, 567–570.

McCalpin, J. P. (1996), *Paleoseismology*, 588 pp., Elsevier, New York.

McCalpin, J. P., and S. P. Nishenko (1996), Holocene paleoseismicity, temporal clustering, and probabilities of future large ($M > 7$) earthquakes on the Wasatch fault zone, Utah, *J. Geophys. Res.*, *101*, 6233–6253.

Niemi, N. A., B. P. Wernicke, A. M. Friedrich, M. Simons, R. A. Bennett, and J. L. Davis (2004), BARGEN continuous GPS data across the eastern Basin and Range province, and implications for fault system dynamics, *Geophys. J. Int.*, *159*, 842–862.

Olig, S. S., G. N. McDonald, B. D. Black, C. B. DuRoss, and W. R. Lund (2004), The Mapleton "megatrench", deciphering 11,000 years of earthquake history on the Wasatch fault near Provo, *Utah Geol. Surv. Notes*, *36-2*, 4–6.

Pechmann, J. C., and W. J. Arabasz (1995), The problem of the random earthquake in seismic hazard analysis: Wasatch Front region, Utah, in *Environmental and Engineering Geology of the Wasatch Front Region: 1995 Symposium and Field Conference*, edited by W. R. Lund, pp. 77–93, Utah Geol. Assoc., Salt Lake City.

Savage, J. C., and W. H. Prescott (1973), Precision of Geodolite distance measurements for determining fault movements, *J. Geophys. Res.*, *78*, 6001–6008.

Savage, J. C., M. Lisowski, and W. H. Prescott (1992), Strain accumulation across the Wasatch fault near Ogden, Utah, *J. Geophys. Res.*, *97*, 2071–2083.

Schwartz, D. P., and K. J. Coppersmith (1984), Fault behavior and characteristic earthquakes: Examples from the Wasatch and San Andreas fault zone, *J. Geophys. Res.*, *89*, 5681–5698.

Shen, Z., D. D. Jackson, and B. X. Ge (1996), Crustal deformation across and beyond the Los Angeles basin from geodetic measurements, *J. Geophys. Res.*, *101*, 27,957–27,980.

Sillard, P., Z. Altamimi, and C. Boucher (1998), The ITRF96 realization and its associated velocity field, *Geophys. Res. Lett.*, *25*, 3223–3226.

Smith, R. B., and W. J. Arabasz (1991), Seismicity of the Intermountain Seismic Belt, in *Neotectonics of North America*, edited by D. B. Slemmons et al., *SMV V-1, Decade Map*, *1*, 185–228, Geol. Soc. Am., Boulder, Colo.

Smith, R. B., and M. L. Sbar (1974), Contemporary tectonic and seismicity of the western United States with emphasis on the Intermountain Seismic Belt, *Geol. Soc. Am. Bull.*, *85*, 1205–1218.

Snay, R. A., R. B. Smith, and T. Soler (1984), Horizontal strain across the Wasatch Front near Salt Lake City, Utah, *J. Geophys. Res.*, *89*, 1113–1122.

Thatcher, W. (1983), Nonlinear strain buildup and the earthquake cycle on the San Andreas fault, *J. Geophys. Res.*, *88*, 5893–5902.

Thatcher, W., G. R. Foulger, B. R. Julian, J. Svarc, E. Quilty, and G. W. Bawden (1999), Present-day deformation across the Basin and Range province, western United States, *Science*, *283*, 1714–1718.

Ward, S. N. (1994), A multidisciplinary approach to seismic hazard in southern California, *Bull. Seismol. Soc. Am.*, *84*, 1293–1309.

White, N. J., J. A. Jackson, and D. P. McKenzie (1986), The relationship between the geometry of normal faults and that of the sedimentary layers in their hanging walls, *J. Struct. Geol.*, *8*, 897–909.

Williams, S. D. P., Y. Bock, P. Fang, P. Jamason, R. M. Nikolaidis, L. Prawirodirdjo, M. Miller, and D. J. Johnson (2004), Error analysis of continuous GPS position time series, *J. Geophys. Res.*, *109*, B03412, doi:10.1029/2003JB002741.

Wong, I., et al. (2002), Earthquake scenario and probabilistic ground shaking maps for the Salt Lake City, Utah, metropolitan area, *Misc. Publ. 02-5*, pp. 1–50, Utah Geol. Surv., Salt Lake City.

Wyatt, F. (1982), Displacement of surface monuments: horizontal motion, *J. Geophys. Res.*, *87*, 979–989.

Zoback, M. L. (1983), Structure and Cenozoic tectonism along the Wasatch fault zone, Utah, in *Tectonics and Stratigraphy of the Eastern Great Basin*, edited by D. M. Miller, V. R. Todd, and K. A. Howard, *Mem. Geol. Soc. Am.*, *157*, 3–27.

W.-L. Chang and R. B. Smith, Department of Geology and Geophysics, University of Utah, Salt Lake City, UT 84112, USA. (wchang@earth.utah.edu)

R. A. Harris, Department of Geology, Brigham Young University, Provo, UT 84602, USA.

C. M. Meertens, UNAVCO, 6350 Nautilus Drive, Boulder, CO 80301, USA.